Supplementary Information

Supramolecular Transparent Plastic Engineering via Covalent-and-Supramolecular Polymerization

Yunfei Zhang,[a] Changyong Cai,[*b] Zhiyuan Guo,[c] Xing Li,[*d] Gai Zhao[*c] & Shengyi Dong[*a]

Y. Zhang, Prof. S. Dong

College of Chemistry and Chemical Engineering, Hunan University, Changsha 410082, China.

Dr. C. Cai

Institute of Bast Fiber Crops, Chinese Academy of Agricultural Sciences, Changsha, Hunan 410205, P. R. China

Prof. X. Li

School of Chemistry and Chemical Engineering, Hainan University, Haikou 570228, China

Z. Guo, Prof. G. Zhao

State Key Laboratory of Mechanics and Control of Mechanical Structures, Nanjing University of Aeronautics and Astronautics, Nanjing 210016, China

*To whom correspondence should be addressed.

E-mail: cyy@hnu.edu.cn; lixing@hainanu.edu.cn; zhaogai@nuaa.edu.cn; dongsy@hnu.edu.cn

Contents

1. Materials and methods

Thioctic acid (**TA**), octylamine (**PA**$_1$), ethylenediamine (**PA**$_2$), diethylenetriamine (**PA**$_3$), triethylenetetramine (**PA**$_4$), tetraethylenepentamine (**PA**$_5$), N-(3-dimethylaminopropyl)-N′-ethylcarbodiimide hydrochloride (EDC) and 4-dimethylaminopyridine (DMAP) were purchased from Shanghai Macklin Biochemical Technology Co., Ltd. Other solvents and materials were commercially obtained and used directly. NMR spectra were collected on a Bruker-AV400 (Germany) with TMS as the internal standard. differential scanning calorimeter (DSC) measurements were obtained by a TAQ200 (American) with a heating rate of 10 ºC from –80 to 200 ºC in nitrogen atmosphere. Powder X-ray diffraction (PXRD) spectra were collected on an Ultima IV (Germany). Infrared (IR) spectra were collected on a Thermo Scientific Nicolet iS50 spectrometer (American). High resolution mass spectrum was recorded on a Orbitrap Exploris 120 (Germany). Dynamic thermomechanical analysis (DMA) was performed on a DMA 8000-PerkinElmer (American) using shear model. Rheology measurements were performed on an Anton Paar MCR 92 (Australia). Nanoindentation results were obtained by an Anton Paar UNHT (Austria). Scanning electron microscopy (SEM) images were collected on a Sigma 300 (Germany). Atomic force microscope (AFM) images were collected on a Bruker (Germany). Small angle X-ray scattering (SAXS) was performed on a Xenocs Xeuss 3.0 (France). The adhesion strength measurements and tensile stress were performed on a HY-0580 electronic tensile testing machine (China). Three-point-bend beam force–displacement curves were performed on a INSTRON 5982/8872/CMT4104/RGM-6300 (American). The hot-pressing process was performed on a PCH-600C (China). Impact resistance is measured by a digital impact tester XBL instrument (GB/T1043-2008).

Method I

Poly[**TA-PA**]$_2$: **TA**: **PA**$_2$ = 2: 1, in molar ratio.

Poly[**TA-PA**]$_3$: **TA**: **PA**$_3$ = 3: 1, in molar ratio.

Poly[**TA-PA**]$_4$: **TA**: **PA**$_4$ = 4: 1, in molar ratio.

Poly[**TA-PA**]$_5$: **TA**: **PA**$_5$ = 5: 1, in molar ratio.

Method Ⅱ

Poly[**TA**]/**PA**$_2$: **TA**: **PA**$_2$ = 2: 1, in molar ratio.

Poly[**TA**]/**PA**$_3$: **TA**: **PA**$_3$ = 3: 1, in molar ratio.

Poly[**TA**]/**PA**$_4$: **TA**: **PA**$_4$ = 4: 1, in molar ratio.

Poly[**TA**]/**PA**$_5$: **TA**: **PA**$_5$ = 5: 1, in molar ratio.

Swelling rate

The swelling rate (S_R) was calculated using the following formula:

$$S_R = \frac{W_t - W_0}{W_0} \times 100\%$$

where W_0 (g) represents the weight of initial poly[**TA**-**PA**]$_5$ and W_t (g) represents the weight of after swelling.

2. Theoretical calculations

The molecular dynamics simulation was carried out using Software Materials Studio from Accelrys, Inc. of USA. Firstly, the molecular structures of poly[**TA**] repeating unit, hexamethyltriethylenetetramine and triethylenetetramine were firstly built using the Materials Visualizer module, and then the structural optimization and dynamical equilibrium were carried out by the Forcite module. The poly[**TA**] with a polymerization degree of 20 and all materials were assembled into a low-density unit cell using Amorphous cell module, which was finally achieved a periodic structure matching with the experimental density. In the geometry optimization for the initial model, the Smart algorithm[1] and COMPASS II force field[2] is used and the van der Waals and Coulomb interactions between molecules are analyzed by the Ewald and Atom-based methods. The system energy is gradually decreased and stabilized by repeated optimization, so that the energy of the system is reduced and stabilized. The energy of the system gradually decreases and tends to stabilize to obtain the optimal geometry. Then the system was annealed from 300 K to 500 K at 50 K intervals to fully relax the structure. Finally, NVT and NPT are used for dynamical equilibrium, NVT is optimized to simulate 1000 ps at 298 K with 1 fs per simulation step and Nose for temperature control, and NPT is optimized to simulate 1000 ps at 298 K with 1 fs per

simulation step and Berendsen for pressure control. Solubility parameters, cohesive energy density, and mechanical properties are obtained in the optimized model analysis.

Stretching of the optimized model is implemented through scripts with each stretch being 5% of the original length, and the model after each stretch is output. The free volume after each stretching can be obtained by calculating the Connelly surface of the molecule through the Atom Volumes & Surfaces module.

All DFT calculations were performed with the Gaussian 16 software. The B3LYP functional was used throughout the entire calculation process. Geometry optimization and frequency calculations were performed using the 6-31+G (d, p) basis set to establish the optimal geometry for each compound. In addition, the DFT-D3 correction was implemented to improve the accuracy of weak interaction calculations.[3,4]

Molecular dynamics simulations were performed using GROMACS 5.1.1.[5] The GAFF force field, encompassing bonds, angles, dihedrals, and Lennard-Jones parameters, were applied to all components.[6] Partial charges were determined using the restrained electrostatic potential (RESP) method at the B3LYP/6-31+G (d, p) level. Electrostatic interactions were calculated using the particle mesh Ewald (PME) method. Equations of motion were solved using the leapfrog integration algorithm with a 2.0 fs time step. A 1.2 nm cutoff distance was employed for van der Waals and electrostatic interactions. The PME method utilized an interpolation order of 4 and a Fourier grid spacing of 0.10 nm.

3. Synthesis of TA-PA$_1$

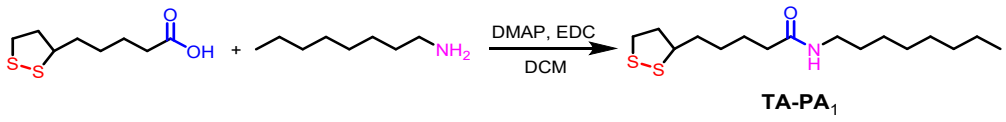

TA-PA$_1$

Scheme S1. Synthesis of **TA-PA$_1$**.

^{1}H NMR (400 MHz, $CDCl_3$, room temperature) δ (ppm): 5.96 (s, 1H), 3.60–3.53 (m, 1H), 3.25–3.08 (m, 4H), 2.50–2.42 (m, 1H), 2.19–2.15 (t, 2H), 1.95–1.86 (m, 1H), 1.73–1.64 (m, 4H), 1.50–1.45 (m, 4H), 1.29–1.26 (m, 10H), 0.89–0.86 (t, 3H); ^{13}C NMR (100 MHz, $CDCl_3$, room temperature) δ (ppm): 172.64, 54.46, 40.25, 39.55, 38.48, 36.54, 34.65, 31.80, 29.68, 29.28, 29.22, 28.92, 26.96, 25.50, 22.65, 14.11.

HRESIMS: m/s calcd for $[M + Na]^+$ $C_{16}H_{31}NOS_2Na$, 340.1739; found 340.1730, error 2.6 ppm.

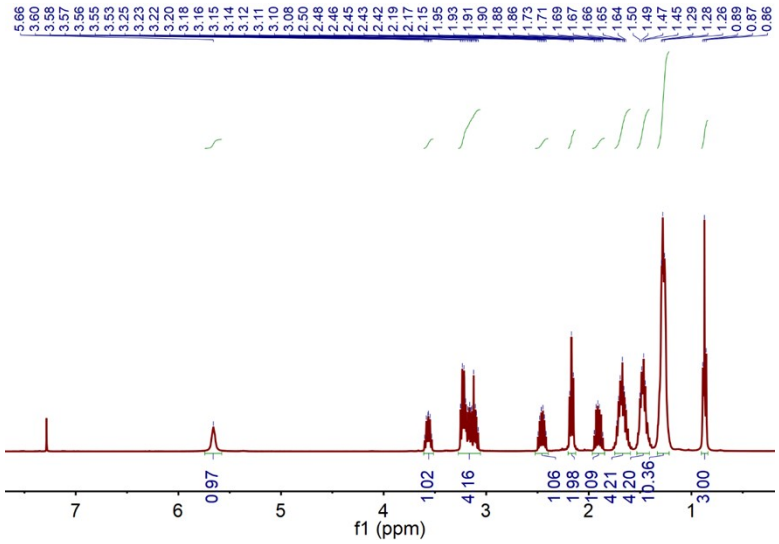

Figure S1. ^{1}H NMR spectrum (400 MHz, $CDCl_3$, room temperature) of **TA-PA$_1$**.

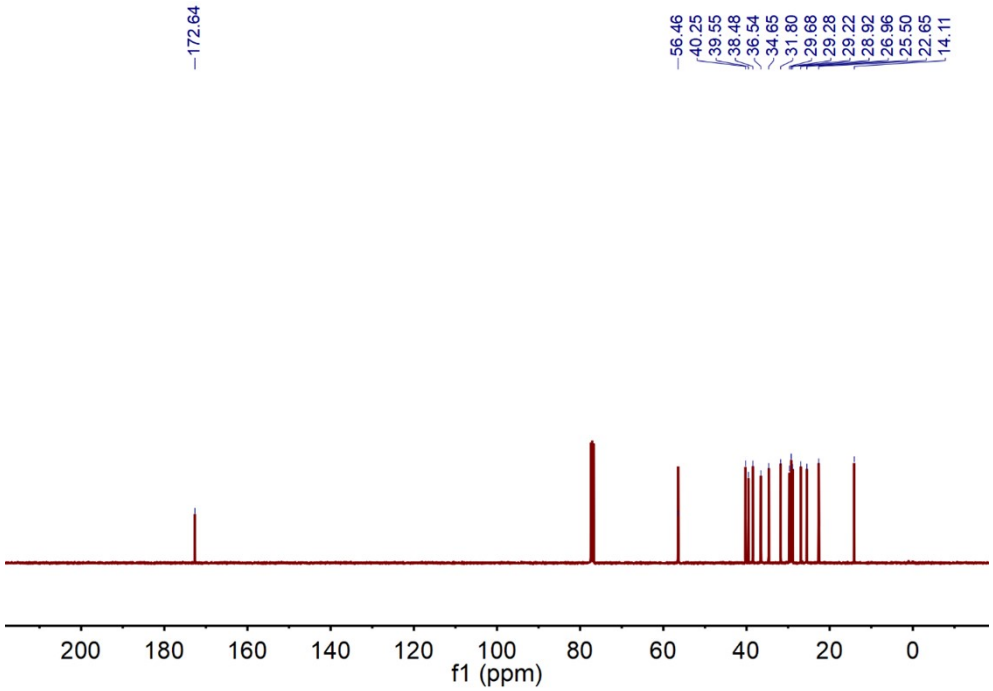

Figure S2. ^{13}C NMR spectrum (100 MHz, $CDCl_3$, room temperature) of **TA-PA$_1$**.

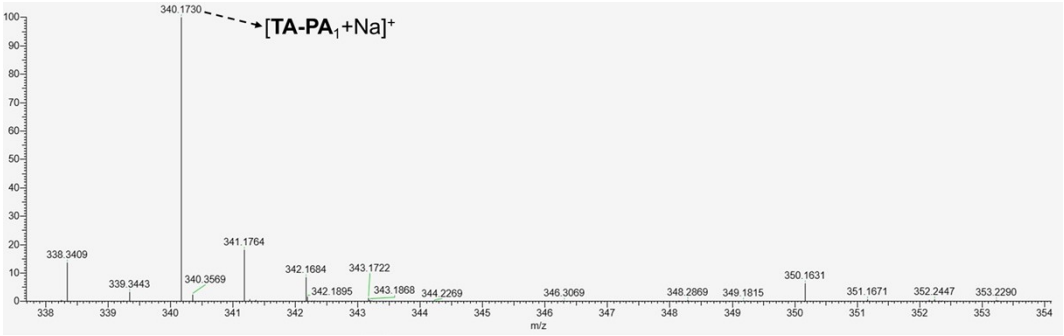

Figure S3. High resolution mass spectrum of compound **TA-PA**$_1$.

4. NMR spectra

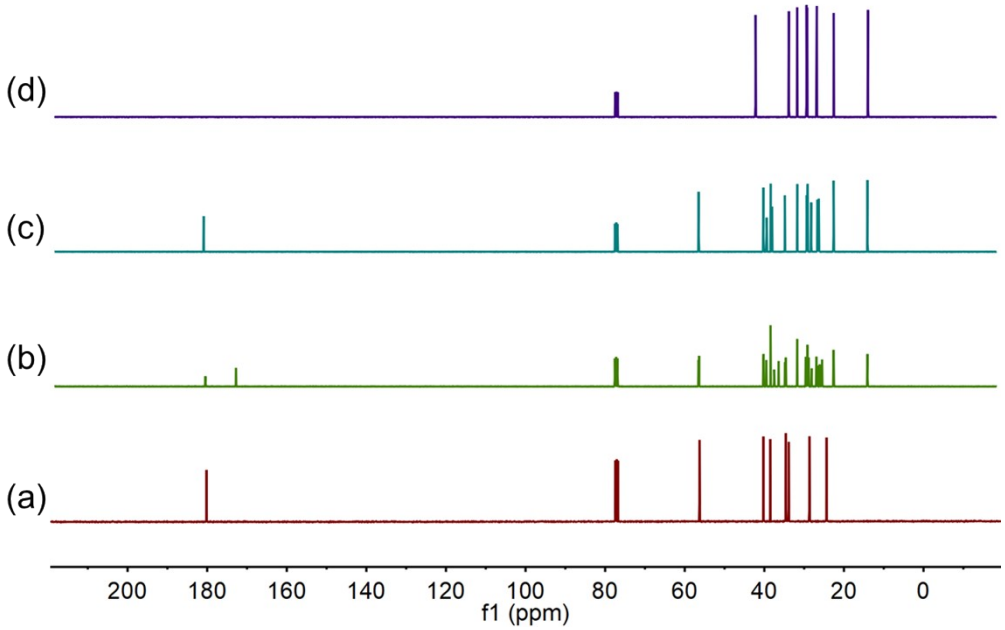

Figure S4. ^{13}C NMR (100 MHz, $CDCl_3$, room temperature): (a) **TA**; (b) poly[**TA-PA**]$_1$; (c) a mixture of **TA** (160 mg/mL) and **PA$_1$** (100 mg /mL); and (d) **PA$_1$**.

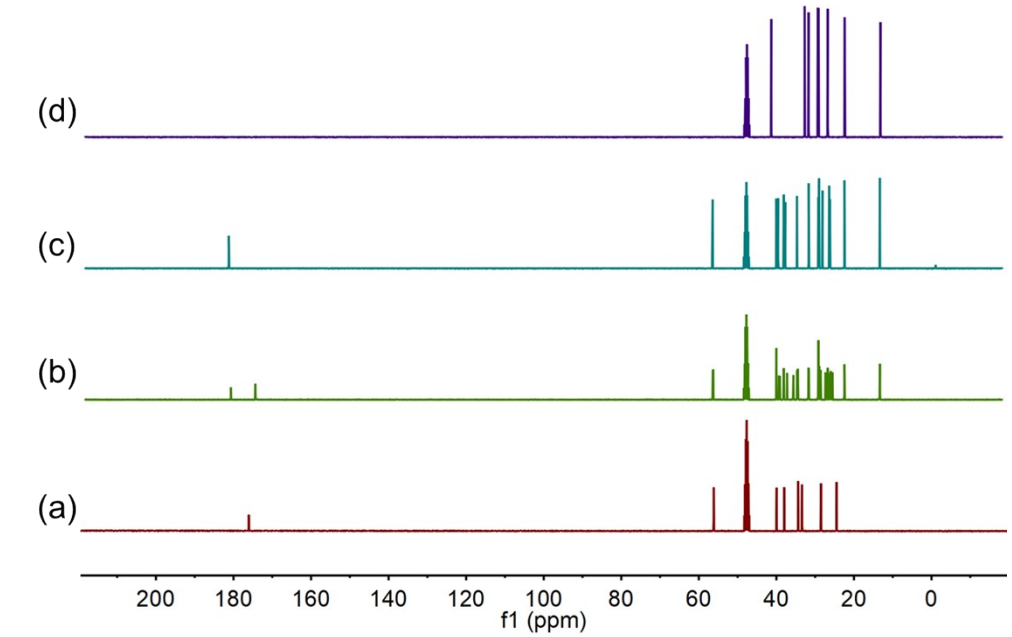

Figure S5. ^{13}C NMR (100 MHz, MeOH-d_4, room temperature): (a) **TA**; (b) poly[**TA**-**PA**]$_1$; (c) a mixture of **TA** (160 mg/mL) and **PA$_1$** (100 mg/mL); and (d) **PA$_1$**.

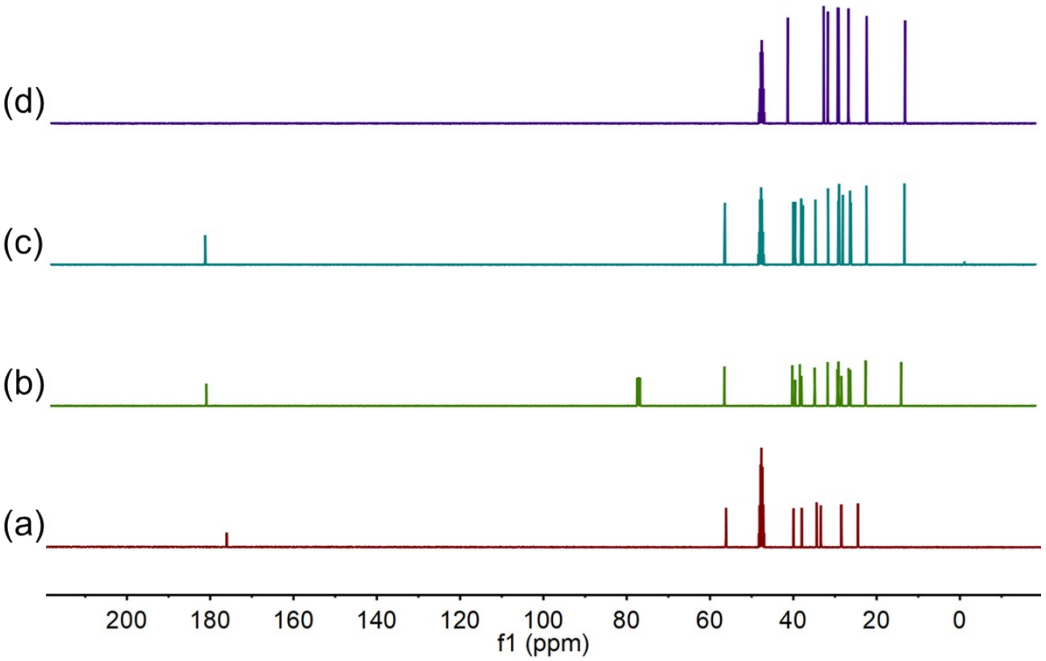

Figure S6. ^{13}C NMR (100 MHz, MeOH-d_4, room temperature): (a) **TA**; (b) poly[**TA**]/**PA$_1$**; (c) a mixture of **TA** (160 mg/mL) and **PA$_1$** (100 mg/mL); and (d) **PA$_1$**.

5. Rheological testing

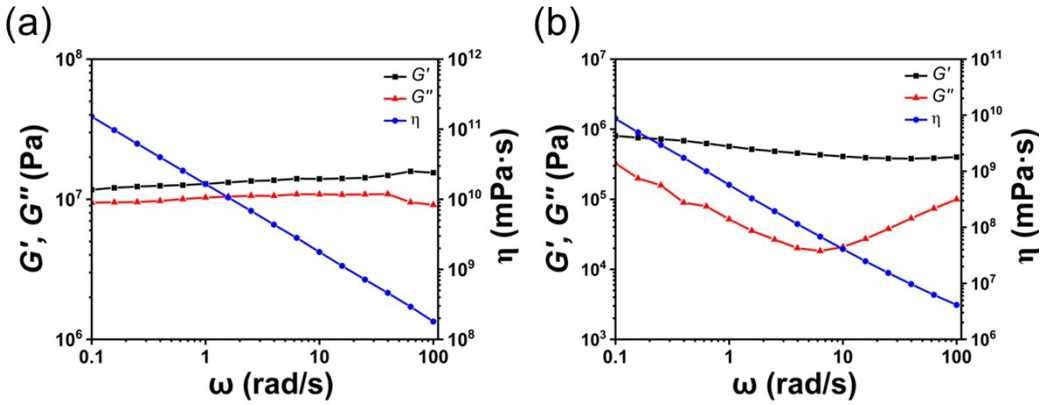

Figure S7. Storage (*G'*), loss (*G''*) moduli and viscosity (η) of poly[**TA-PA**]$_3$ at different temperature: (a) 25 °C and (b) 100 °C.

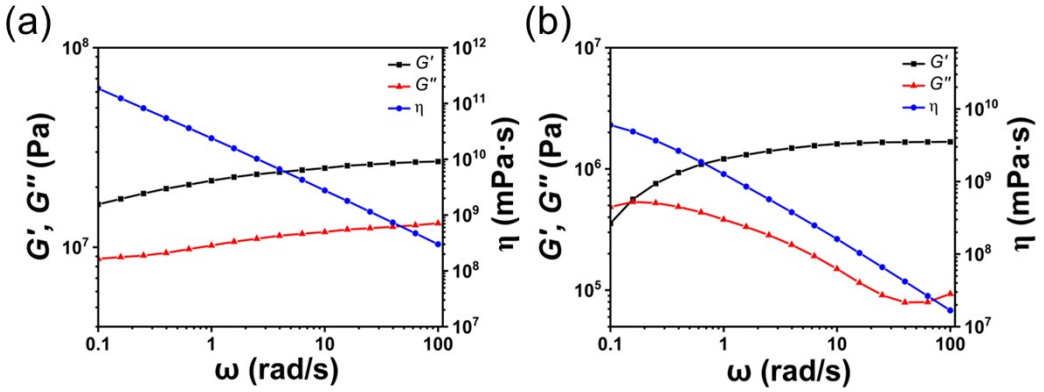

Figure S8. Storage (*G'*), loss (*G''*) moduli and viscosity (η) of poly[**TA-PA**]$_4$ at different temperature: (a) 25 °C and (b) 100 °C.

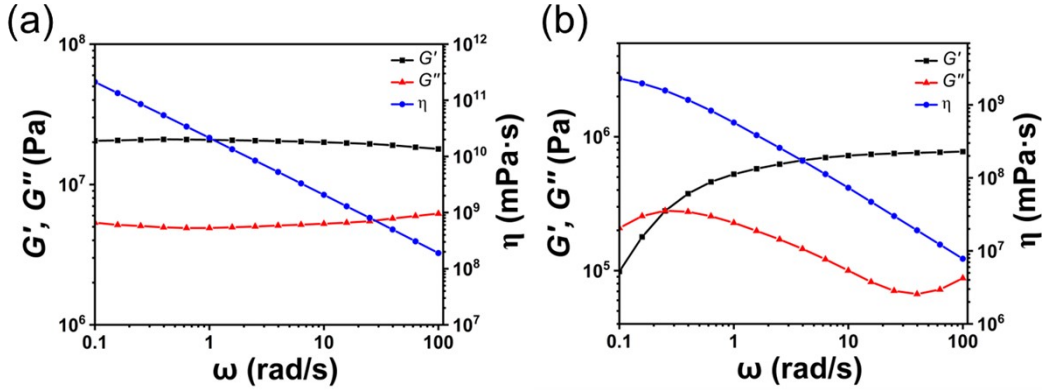

Figure S9. Storage (*G'*), loss (*G''*) moduli and viscosity (η) of poly[**TA-PA**]$_5$ at different temperature: (a) 25 °C and (b) 100 °C.

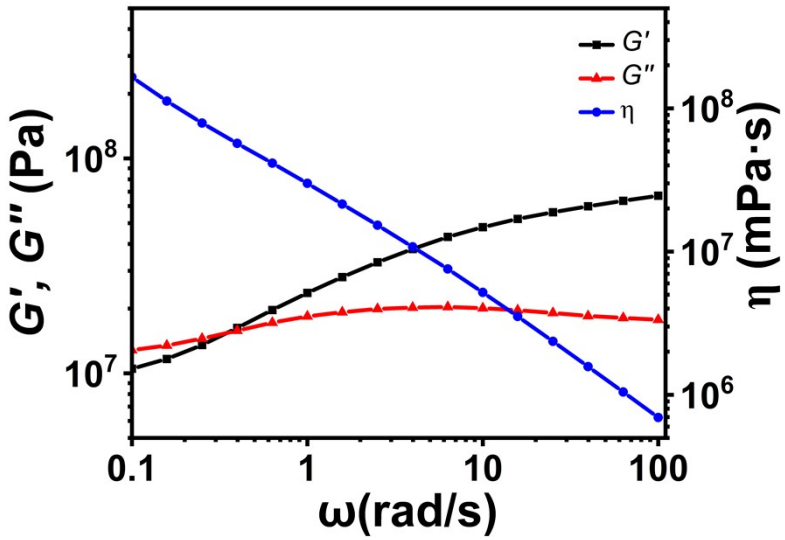

Figure S10. Storage (*G'*), loss (*G''*) moduli and viscosity (η) of poly[**TA**]/**PA**$_5$.

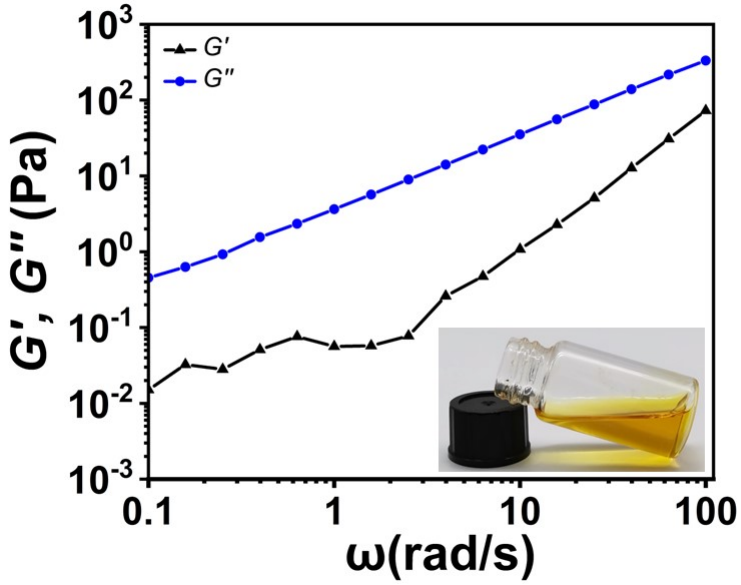

Figure S11. Storage (*G'*) and loss (*G''*) moduli of poly[**TA**]/**TMA** (the photo of poly[**TA**]/**TMA** after cooling).

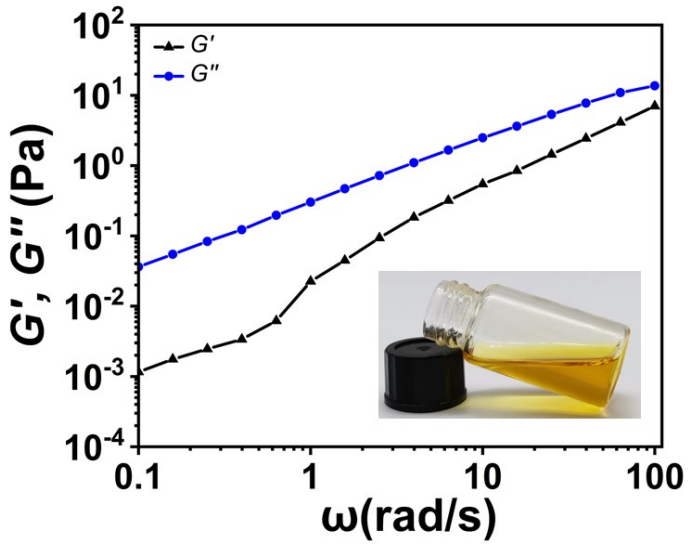

Figure S12. Storage (*G'*) and loss (*G''*) moduli of poly[**TA**]/**TEG** (the photo of poly[**TA**]/**TEG** after cooling).

6. Theoretical calculations

Table S1. Average number bonds and binding energy of different system.

System	Average number bonds	Binding energy (kcal/mol)
1 + **2**	248.393	-2134.45
1 + **3**	213.068	-8553.75

Table S2. Cohesive energy density of different system.

System	Cohesive energy density ($\times 10^8$ J/m^3)	Solubility parameter (J/m^3)$^{0.5}$
Poly[**TA**]/**TMA**	4.45	21.08
Poly[**TA**]/**PA**$_4$	5.19	22.77
Poly[**TA-PA**]$_4$-2	4.96	22.27
Poly[**TA-PA**]$_4$-6	4.70	21.67
Poly[**TA-PA**]$_4$-10	4.22	20.53

Note: 2, 6, 10 represents the number of cross-linked amide groups in poly[**TA-PA**]$_4$.

7. Adhesion behavior and adhesion mechanism

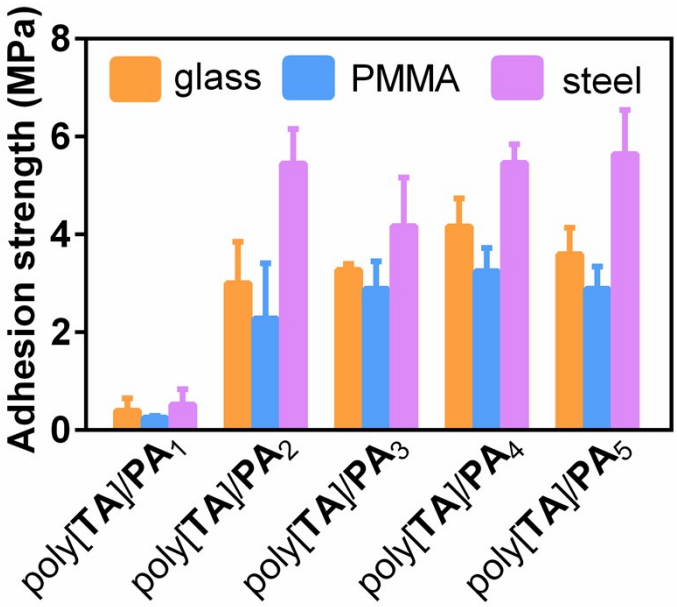

Figure S13. The adhesion strengths of poly[**TA**]/**PA**$_1$, poly[**TA**]/**PA**$_2$, poly[**TA**]/**PA**$_3$, poly[**TA**]/**PA**$_4$, and poly[**TA**]/**PA**$_5$ at room temperature.

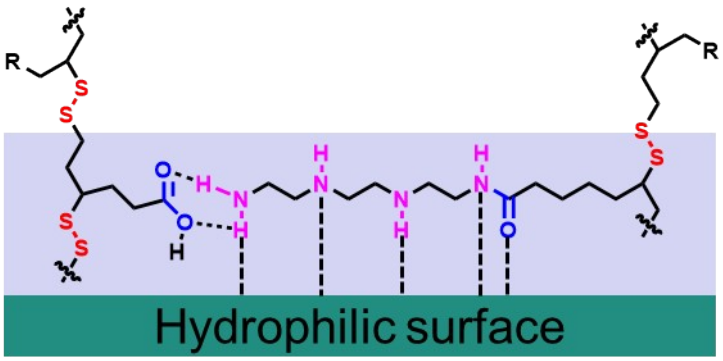

Figure S14. The possible adhesion mechanism of poly[**TA-PA**]$_s$.

Generally, the adhesion mechanism of poly[**TA-PA**] contained two individual aspects, the cohesion behavior of poly[**TA-PA**] (intermolecular interactions and mechanical toughness of poly[**TA-PA**], without any interaction with the adhered surface) and the adhesion behavior of poly[**TA-PA**] to the surface (the interactions between poly[**TA-PA**] adhesive layer and the adhered surface).

Cohesion behavior: cohesion performance is the intrinsic property of an adhesive, and is not related to the adhered surface. There are two factors that determine the cohesion strength, cohesion energy (non-covalent intermolecular interactions) and

mechanical toughness (mechanical property of the adhesive layer). Usually, cohesion energy density (CED, providing a measure of the intermolecular attraction forces in the material and describing the magnitude of intermolecular forces) is used to evaluate the intermolecular interactions of an adhesive. Due to the multiple hydrogen bonds, poly[**TA-PA**] had a high CED of 4.96×10^8 J/m^3, indicating the strong cohesion interactions in it (Figure 2c). Meanwhile, poly[**TA-PA**] adhesive layer had the high Yound's moduli, low enongation rate, high hardness, and high mechanical toughness, meaning that the adhesive layer is tough, rather than fraigle or soft (Figure 4d,5b). Therefore, poly[**TA-PA**] layer can highly withstand to the shear force in the weight-loding process, and keep its structural integrity.

Adhesion behavior: here we used the adhesion to glass as an example. Poly[**TA-PA**] had multiple hydrophilic groups, including carboxylic acid, amide, and amine, and can form hydrogen bonds with the hydrophilic units of glass to realize a good adhesion, which was confirmed by the simulations (Figure S15,16).

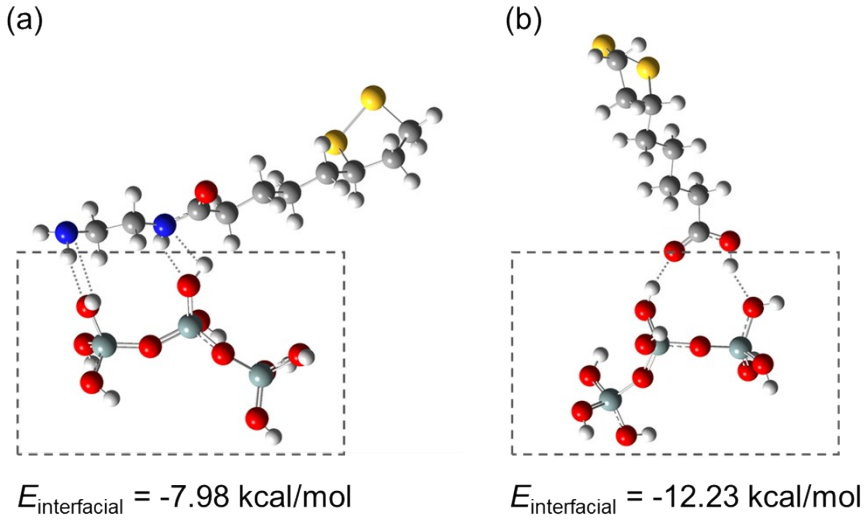

Figure S15. The calculated interaction energies of **1**-glass and **3**-glass. The red, blue, white, yellow, grey, and cyan spheres represent the O, N, H, S, C, and Si, respectively.

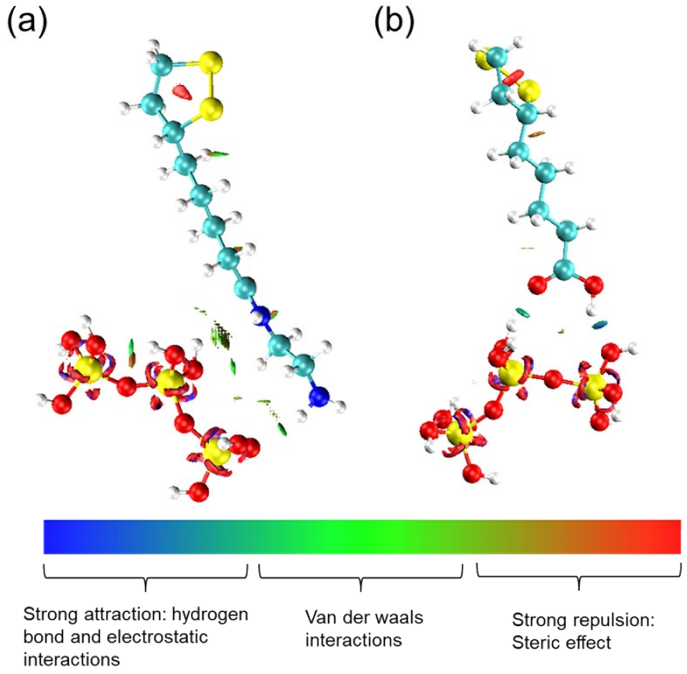

Figure S16. Visualization of non-covalent interactions of **1**-glass and **3**-glass. The blue, green and red regions represent strong electrostatic interactions, dispersive attractive interactions, and steric repulsion, respectively.

8. Transmittance and structural characterizations

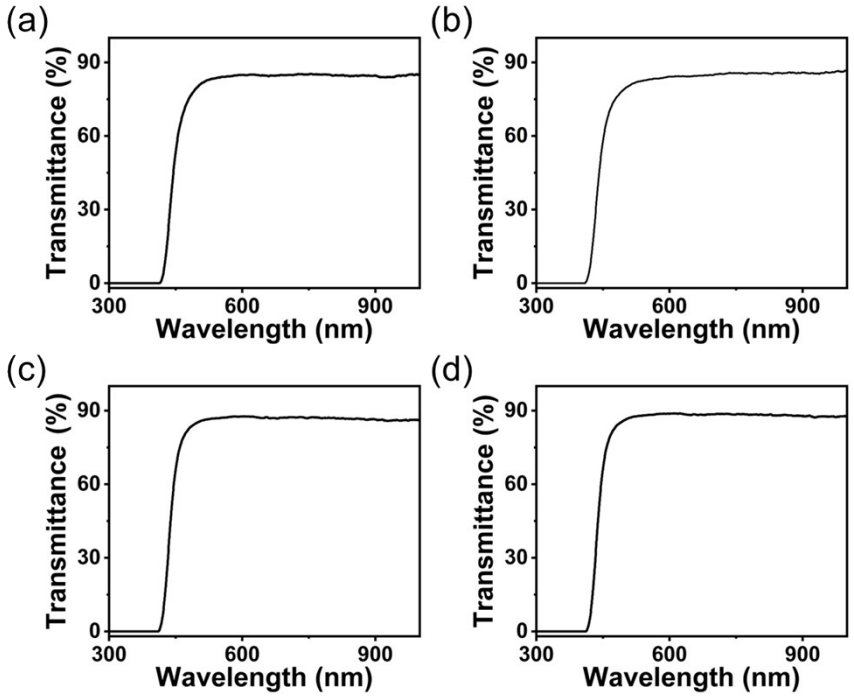

Figure S17. Transmittances: (a) poly[**TA-PA**]$_2$; (b) poly[**TA-PA**]$_3$; (c) poly[**TA-PA**]$_4$; and (d) poly[**TA-PA**]$_5$.

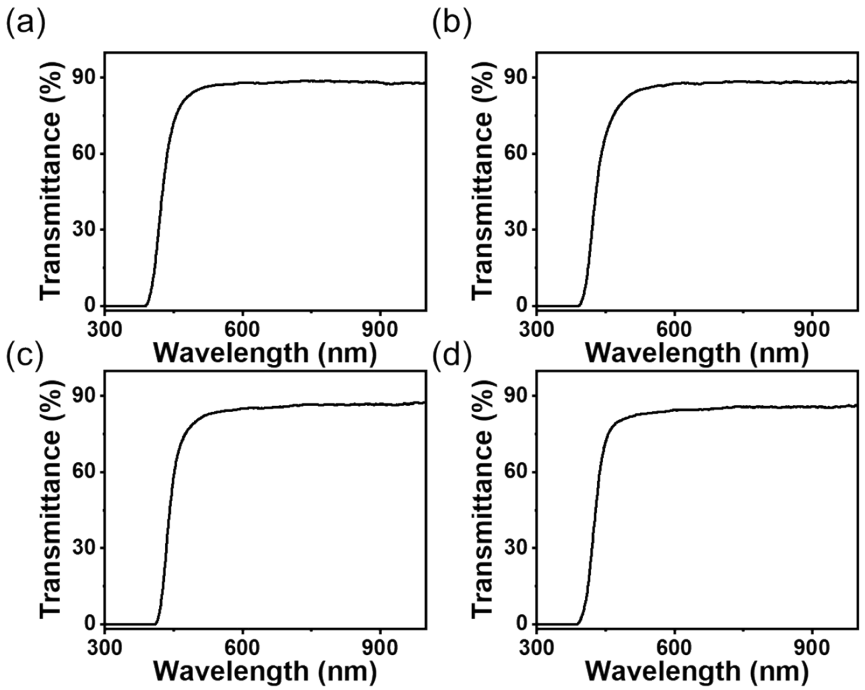

Figure S18. Transmittances: (a) poly[**TA**]/**PA**$_2$; (b) poly[**TA**]/**PA**$_3$; (c) poly[**TA**]/**PA**$_4$; and (d) poly[**TA**]/**PA**$_5$.

Figure S19. Poly[**TA-PA**]$_4$ model.

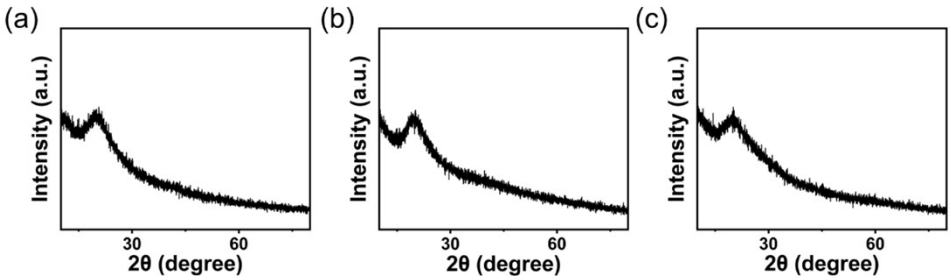

Figure S20. PXRD spectra: (a) poly[**TA-PA**]$_3$; (b) poly[**TA-PA**]$_4$; and (c) poly[**TA-PA**]$_5$.

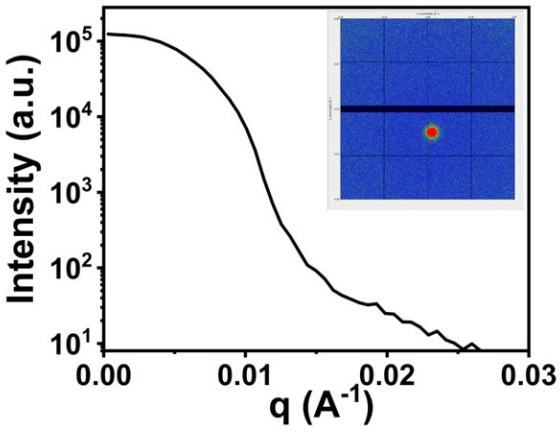

Figure S21. SAXS spectrum of poly[**TA-PA**]$_4$.

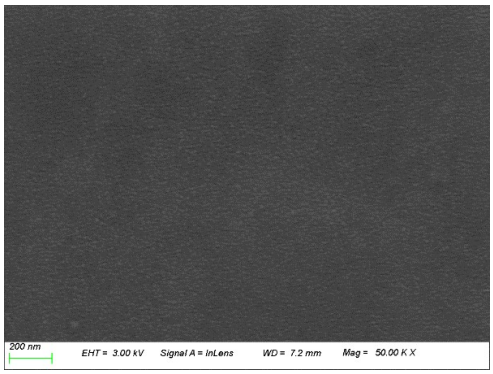

Figure S22. SEM image of poly[**TA-PA**]$_4$.

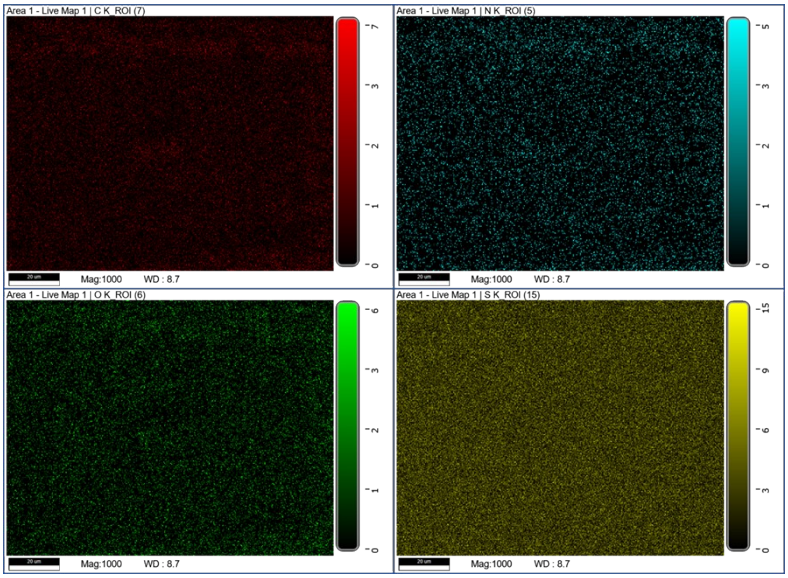

Figure S23. EDS (mapping) images (C, N, O, and S) of poly[**TA-PA**]$_4$.

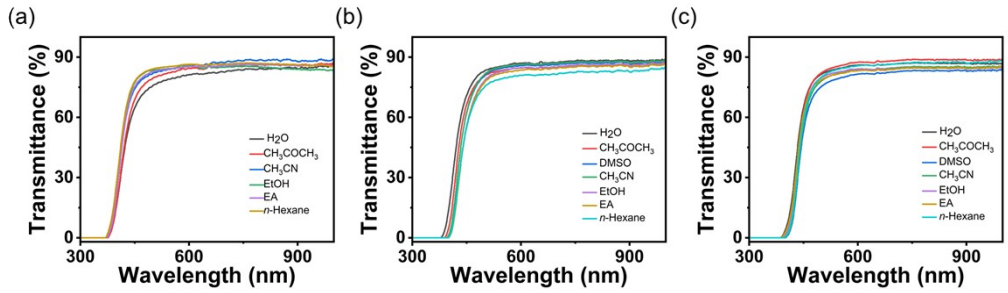

Figure S24. Transmittances in organic solvents: (a) poly[**TA-PA**]$_2$; (b) poly[**TA-PA**]$_3$; and (c) poly[**TA-PA**]$_5$.

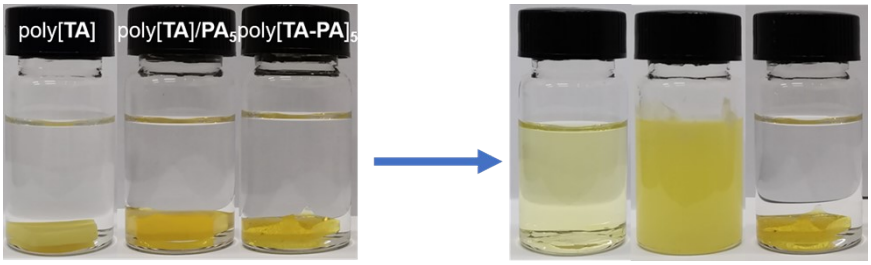

Figure S25. Poly[**TA**], poly[**TA**]/**PA**$_5$, and poly[**TA-PA**]$_5$ in EtOH.

Table S3. The contact angle of different poly[**TA-PA**]$_s$.

Poly[**TA-PA**]$_s$	Contact angle (°)
Poly[**TA-PA**]$_2$	74.72
Poly[**TA-PA**]$_3$	73.58
Poly[**TA-PA**]$_4$	70.48
Poly[**TA-PA**]$_5$	72.91

Table S4. Swelling rate (wt%) of poly[**TA-PA**]$_5$ in different solvents at different times.

Solvent	1 h	16 h	360 h
H_2O	0.29	1.00	1.00
n-Hexane	0.05	0.01	0.01
EtOH	0.01	0.63	0.72
EA	0.04	0.10	0.10
CH_3CN	0.07	0.02	0.24
DMSO	0.02	0.02	0.06

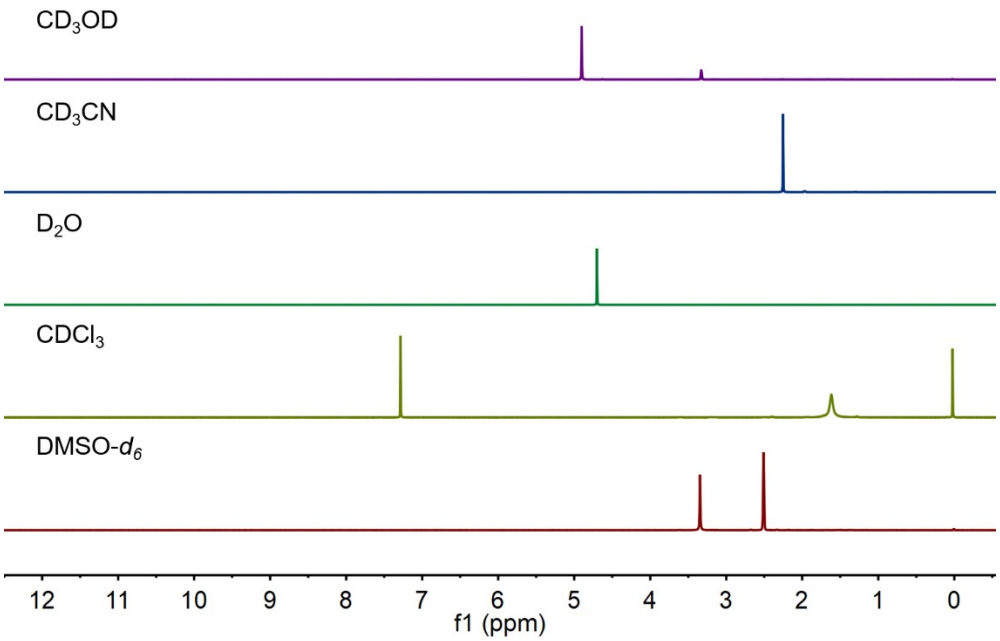

Figure S26. The ^{1}H NMR (400 MHz, room temperature) of poly[**TA-PA**]$_5$ after stored in different solvents for 72 h.

As shown in Figure S26, only water residue and solvent are observed from their ^{1}H NMR spectra.

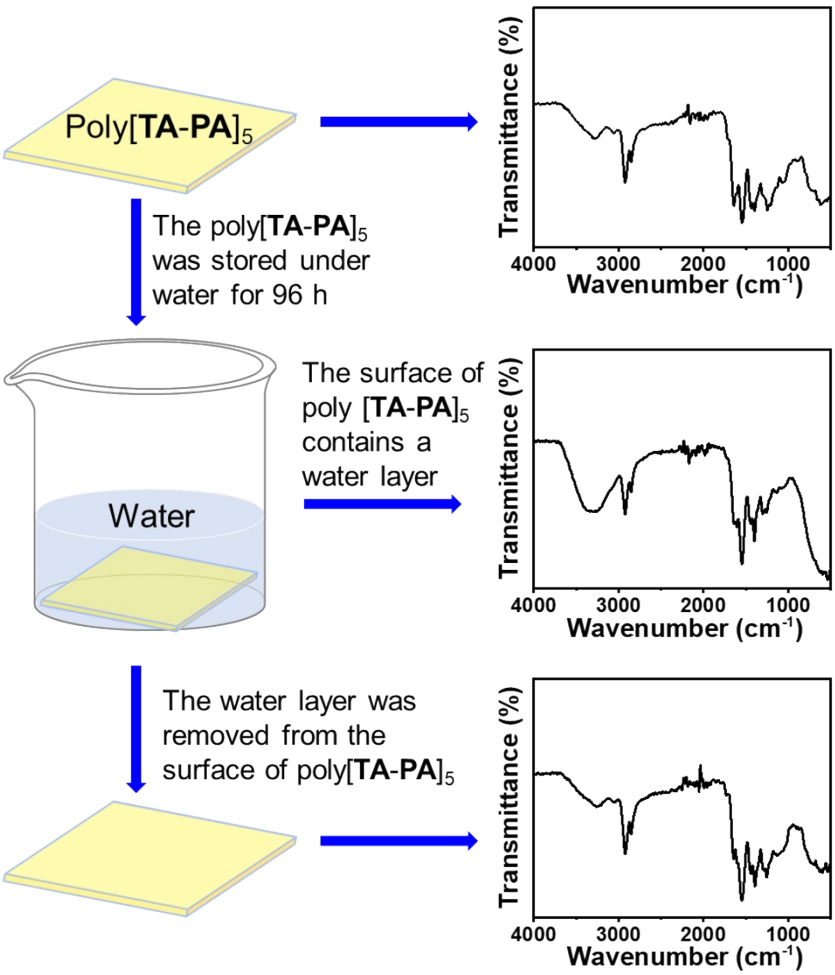

Figure S27. The FT-IR spectra of poly[**TA-PA**]$_5$.

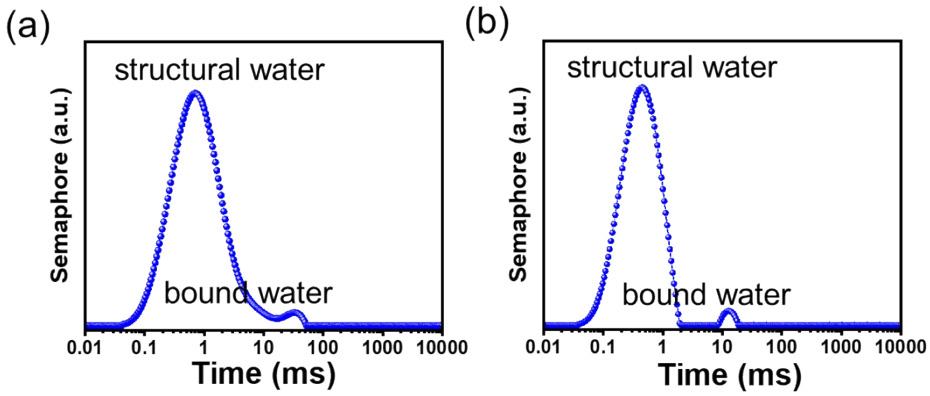

Figure S28. The low-field NMR spectra: (a) poly[**TA-PA**]$_5$ and (b) the surface of poly[**TA-PA**]$_5$ cleaned by a blotting paper after stored under water for 96 h.

The surface of poly[**TA-PA**] is hydrophilic, which was proved by the contact angle measurments (< 75 °, Table S3). The poly[**TA-PA**]$_s$ affinity for water can be ascribed

to the hydrophilic groups, such as carboxylic acid, amine, and amide groups on the surface of poly[**TA-PA**]. However, the hydrophilic surface did not mean that poly[**TA-PA**] is water soluble. Poly[**TA-PA**] shows several unique structural features: a) poly[**TA-PA**] contains polymeric structures, that are poly[**TA**] by the ring-opening polymerization of **TA**; b) poly[**TA-PA**] is covalently (amide groups, irreversible) and non-covalently cross-linked (hydrogen bonds, reversible), and behaves as a thermosetting material. Those structural characteristics demonstrate that poly[**TA-PA**] is a type of thermosetting polymers. Due to the highly dense three dimensional network, water molecules only can form hydrogen bonding with the polar groups from the surface of poly[**TA-PA**] and fail to diffuse into the interior part of poly[**TA-PA**].

Poly[**TA-PA**] samples were stored under water for 360 h, during which no swelling phenomena were observed. This observation demonstrated the good water stability of poly[**TA-PA**]. With this information in mind, IR experiments were performed to investigate the interaction between water and poly[**TA-PA**]. Obvious water absorption band was found from the IR spectrum of water-treated poly[**TA-PA**] (poly[**TA-PA**] sample was directly moved from water and its surface was not cleaned by a blotting paper). When the water layer was removed from the surface of poly[**TA-PA**] by a blotting paper, the recorded IR spectrum was quite close to that of water-untreated poly[**TA-PA**]. By analyzing these observations, it was suggested that water cannot diffusing into the interior part of poly[**TA-PA**].

More experiments were taken to confirm this assumption. Two poly[**TA-PA**] samples (one was stored under water for 96 h, then removed from water and its surface was cleaned by a blotting paper; the other was not treated with water and used directly for NMR test) were prepared for the low-field NMR (LT-NMR) tests. Their LT-NMR spectra were similar and free water was not found ($>$ 1000 ms). This comparison further confirmed that water molecules did not diffuse into the interior part of poly[**TA-PA**].

9. Mechanical properties

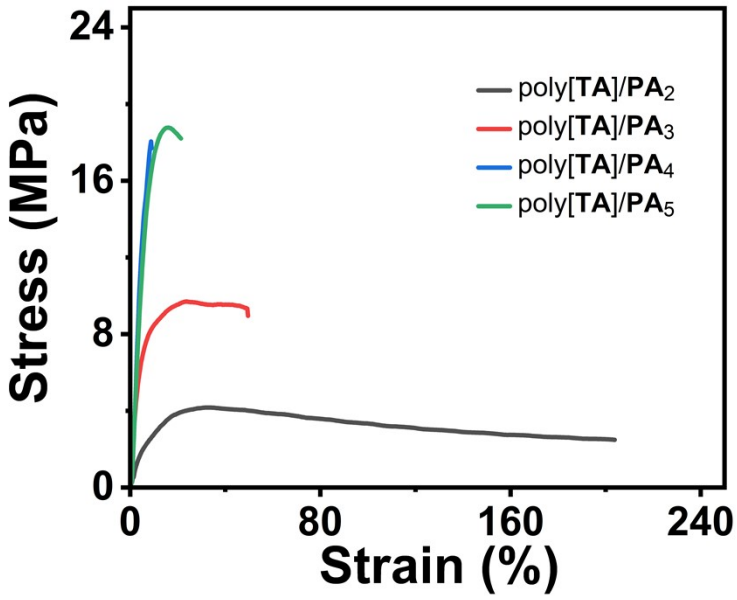

Figure S29. Stress-strain curves of poly[**TA**]/**PA**$_2$, poly[**TA**]/**PA**$_3$, poly[**TA**]/**PA**$_4$, and poly[**TA**]/**PA**$_5$.

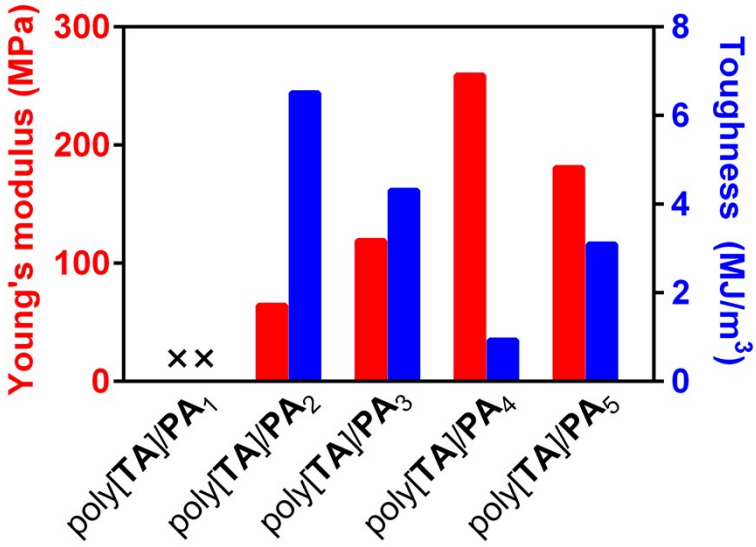

Figure S30. Young's moduli and toughness of poly[**TA**]/**PA**.

Table S5. Comparison of our work and previous research studies.

Reference	Tensile Stress (MPa)	Transmittance
Ref. 7	4.15	transparent
Ref. 8	39.2	transparent
Ref. 9	0.27	opaque
Ref. 10	0.5	opaque
Ref. 11	6.44	opaque
Ref. 12	6.03	opaque
Ref. 13	9.8	transparent
This Work	45.51	transparent

Table S6. Bulk modulus of poly[**TA**], poly[**TA-PA**]$_4$ and **PA**$_4$ at 298 K.

	Bulk modulus Reuss (GPa)	Bulk modulus Voigt (GPa)	Bulk modulus Hill (GPa)
Poly[**TA**]+**PA**$_4$	4.8858	4.9692	4.9275
Poly[**TA-PA**]$_4$+**PA**$_4$	5.9419	6.1543	6.0481

Table S7. Shear modulus of poly[**TA**], poly[**TA-PA**]$_4$ and **PA**$_4$ at 298 K.

	Shear modulus Reuss (GPa)	Shear modulus Voigt (GPa)	Shear modulus Hill (GPa)
Poly[**TA**]+**PA**$_4$	2.1738	2.2381	2.206
Poly[**TA-PA**]$_4$+**PA**$_4$	2.9848	3.1446	3.0647

Table S8. Young's modulus of poly[**TA**], poly[**TA-PA**]$_4$ and **PA**$_4$ at 298 K.

	Young's Modulus X (GPa)	Young's Modulus Y (GPa)	Young's Modulus Z (GPa)
Poly[**TA**]+**PA**$_4$	5.2869	5.5247	4.7349
Poly[**TA-PA**]$_4$+**PA**$_4$	8.8527	6.4267	8.9534

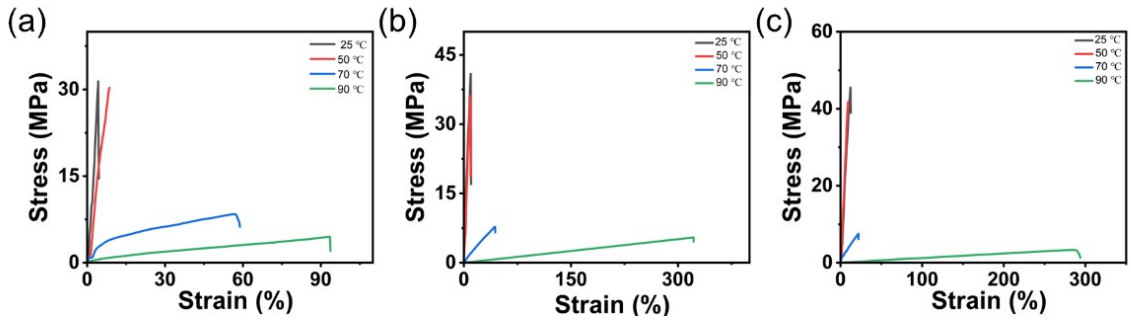

Figure S31. Stress-strain curves of poly[**TA-PA**] at different temperatures: (a) poly[**TA-PA**]$_3$; (b) poly[**TA-PA**]$_4$; and (c) poly[**TA-PA**]$_5$.

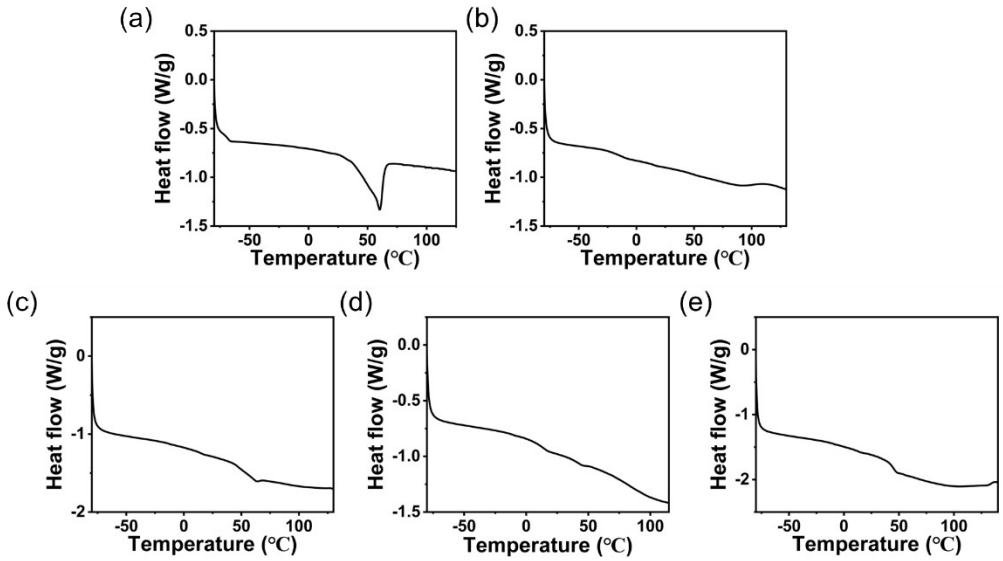

Figure S32. DSC measurements: (a) poly[**TA-PA**]$_1$; (b) poly[**TA-PA**]$_2$; (c) poly[**TA-PA**]$_3$; (d) poly[**TA-PA**]$_4$; and (e) poly[**TA-PA**]$_5$.

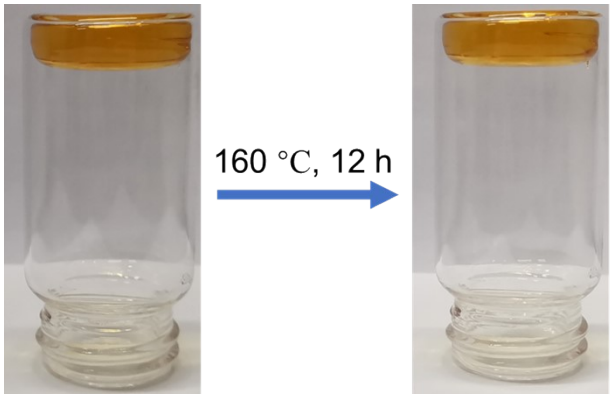

Figure S33. Photos of poly[**TA-PA**]$_5$ at 160 °C.

Figure S34. Photos of poly[**TA**]/**PA**$_5$ at 135 °C.

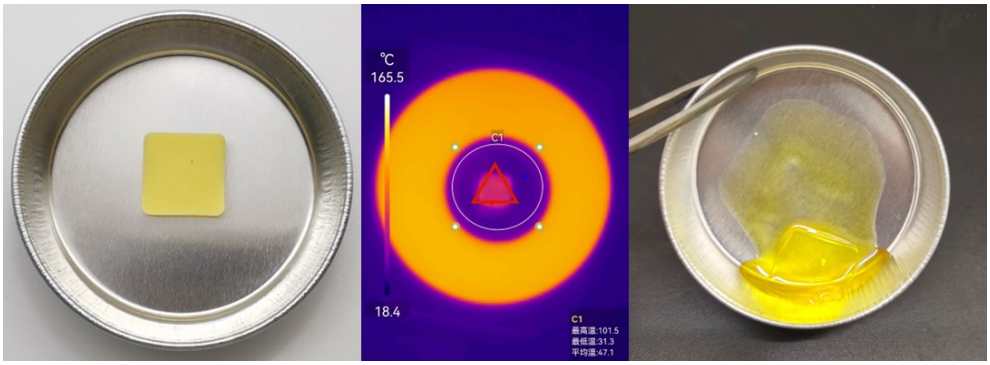

Figure S35. Photos of poly[**TA**] at 100 °C.

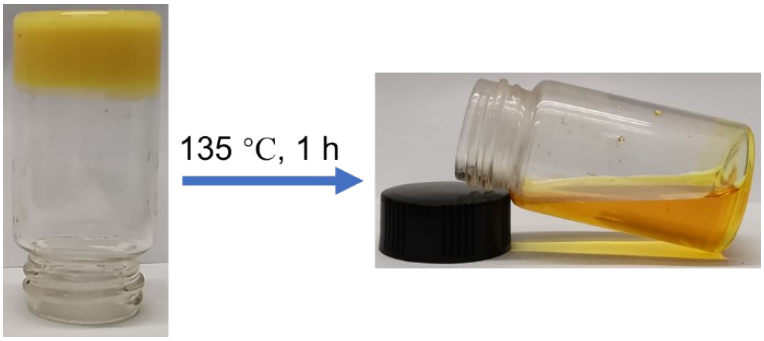

Figure S36. Photos of poly[**TA**] at 135 °C.

One of the typical characteristics of thermosetting materials that distinguish them from thermoplastic materials is their unique heating properties (Figure S33-36). Poly[**TA**], poly[**TA**]/**PA**, and poly[**TA-PA**] were prepared according to the preparation protocol in maintext of this manuscript. Remarkable and reversible phase transitions from a solid state to the liquid state were observed from poly[**TA**] and poly[**TA-PA**] in the heating tests, indicating that both poly[**TA**] and poly[**TA-PA**] belonged to thermoplastics. In contrast, no phase transition of poly[**TA-PA**] was found even when the heating

temperature was above 160 °C (Figure S33). Further increasing the heating temperature only led to the decomposition of poly[**TA-PA**] instead of the occurrence of the liquid-type of poly[**TA-PA**].

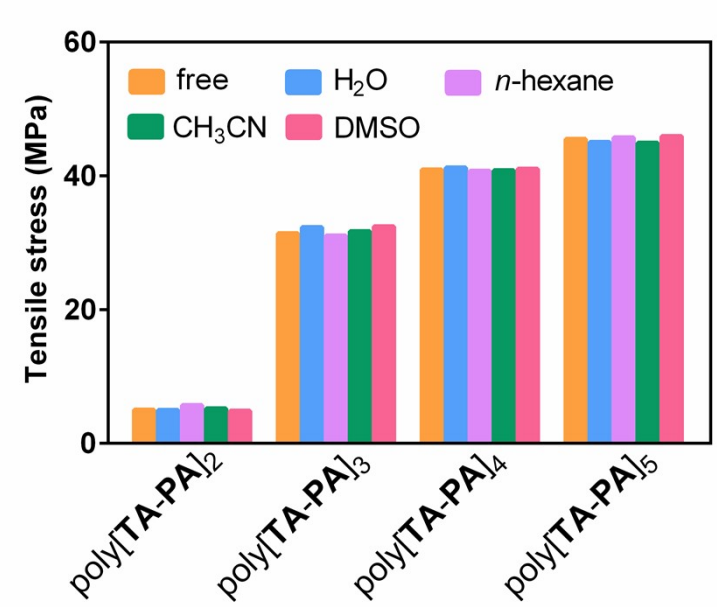

Figure S37. The tensile stress of poly[**TA-PA**]$_s$ after stored in different solutions for 48 h.

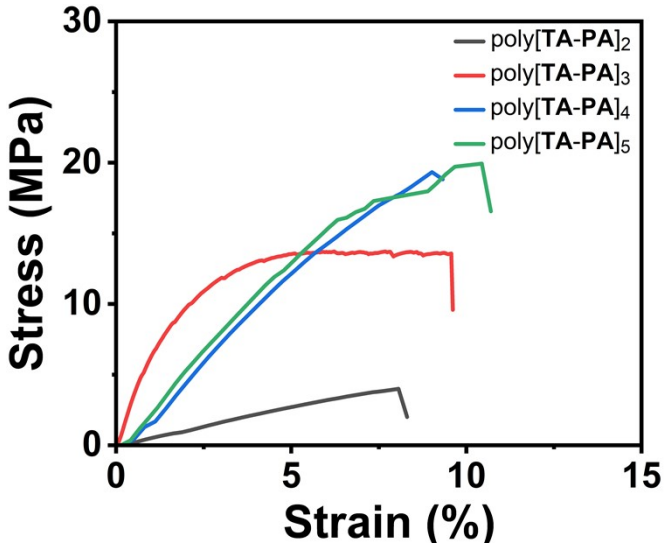

Figure S38. Stress-strain curves of poly[**TA-PA**]$_2$, poly[**TA-PA**]$_3$, poly[**TA-PA**]$_4$, and poly[**TA-PA**]$_5$ under –60 °C.

10. Three-point-bend beam force–displacement curves

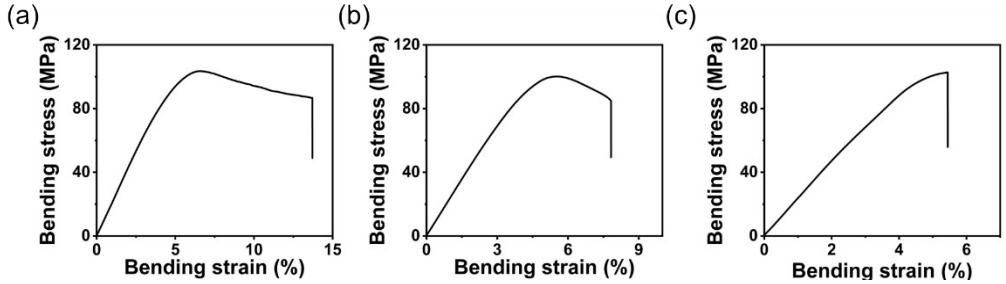

Figure S39. Three-point-bend beam force–displacement curves: (a) poly[**TA-PA**]$_3$; (b) poly[**TA-PA**]$_4$; and (c) poly[**TA-PA**]$_5$.

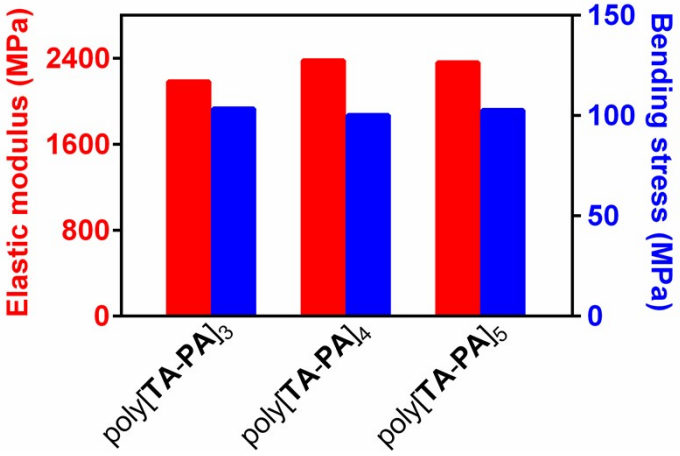

Figure S40. Elastic moduli and bending stress of poly[**TA-PA**]$_3$, poly[**TA-PA**]$_4$, and poly[**TA-PA**]$_5$.

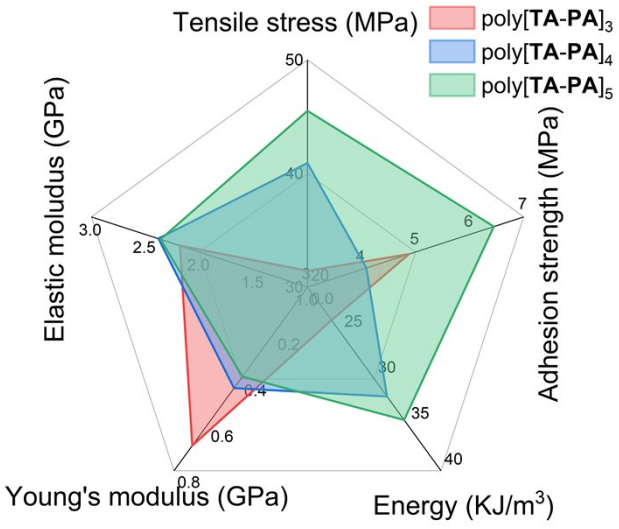

Figure S41. The tensile stress, adhesion strength, energy, Young's moduli, and elastic modulus of poly[**TA-PA**].

Table S9. Comparisons between poly[**TA-PA**]$_s$, PMMA, and PC.

	Poly[**TA-PA**]$_s$	PMMA[14]	PC[14]
Shore (HD)	74.00	65	82
Rebound rate (%)	51.45	43.47	41.30
Tensile stress (MPa)	45.51	55.34	77.58
Bending stress (MPa)	102.67	86.02	97.27
Elastic modulus (GPa)	2.36	2.60	2.41
Transmittance (%)	88.80	91.70	93.10

11. Nanoindentation

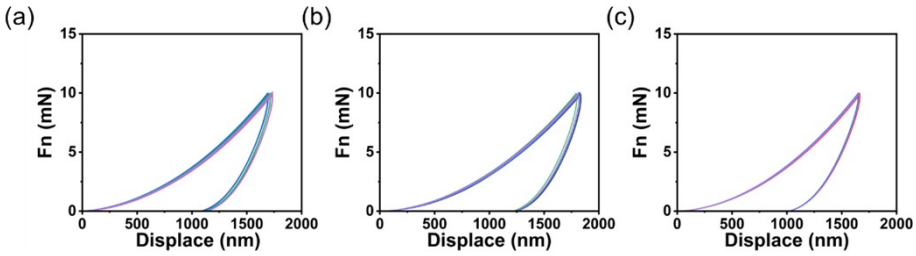

Figure S42. Nanoindentation measurements: (a) poly[**TA-PA**]$_3$; (b) poly[**TA-PA**]$_4$; and (c) poly[**TA-PA**]$_5$.

12. Atomic Force Microscope and mechanical comparison

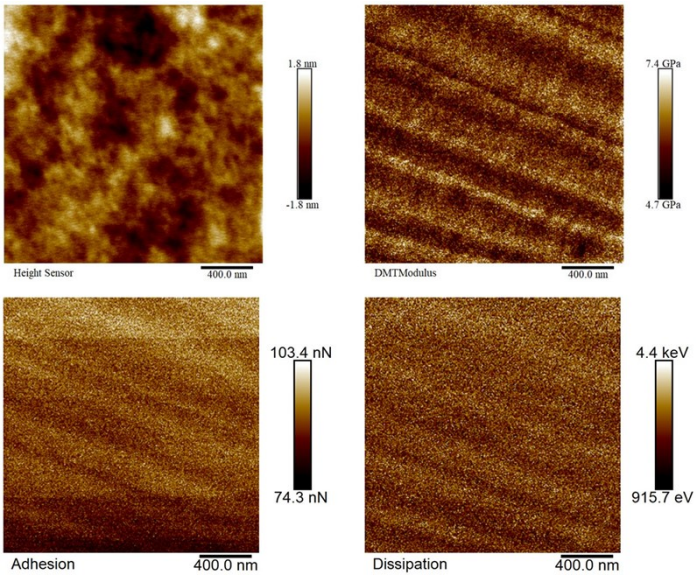

Figure S43. AFM images of poly[**TA-PA**]$_4$.

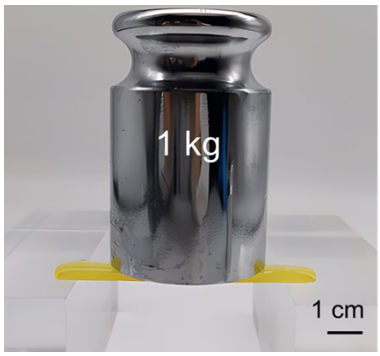

Figure S44. Weight loading test of poly[**TA-PA**]$_4$.

13. References

1. J. Shi, F. Liu, G. Zhang, J. Luo, and J. Bai, *J. Biomed. Opt.*, 2014, **4**, 19.
2. H. Sun, Z. Jin, C. Yang, R. L. C. Akkermans, S. H. Robertson, N. A. Spenley, S. Miller, and S. M. Todd, *J. Mol. Model.*, 2016, **2**, 22.
3. R. Krishnan, J. S. Binkley, R. Seeger, J. A. Pople, *J. Chem. Phys.*, 1980, **72**, 650–654.
4. S. Grimme, S. Ehrlich, L. Goerigk, *J. Comp. Chem.*, 2011, **32**, 1456–1465.
5. D. Van der Spoel, E. Lindahl, B. Hess, G. Groenhof, A. E. Mark, J. C. Berendsen, *J. Comput. Chem.*, 2005, **26**, 1701−1718.
6. J. M. Wang, R. M. Wolf, J. W. Caldwell, P. A. Kollman, D. A. Case, *J. Comput. Chem.*, 2004, **25**, 1157−1174.
7. H. Qiao, B. Wu, S. Sun, and P. Wu, *J. Am. Chem. Soc.*, 2024, **146**, 7533–7542.
8. C. Cui, F. Wang, X. Chen, T. Xu, Z. Li, K. Chen, Y. Guo, Y. Cheng, Z. Ge, and Y. Zhang, *Adv. Funct. Mater.*, 2024, **34**, 2315469.
9. K.-X. Hou, S.-P. Zhao, D.-P. Wang, P.-C. Zhao, C.-H. Li, and J.-L. Zuo, *Adv. Funct. Mater.*, 2021, **31**, 2107006.
10. C. Dang, Y. Shao, S. Ding, H. Qi, and W. Zhai, *Adv. Mater.*, 2024, **36**, 2406967.
11. Y. Zhang, C. Cai, K. Xu, X. Yang, L. Yu, L. Gao, and S. Dong, *Mater. Horiz.*, 2024, **11**, 1315–1324.
12. C. Cai, S. Wu, Y. Zhang, F. Li, Z. Tan, and S. Dong, *Adv. Sci.*, 2022, **9**, 2203630.
13. M. Chen, R. Yang, H. Wu, Q. Wang, C. Shi, S.-W. Zhou, D. Yang, F.-Y. Liu, H.

Tian, and D. Qu, *Angew. Chem. Int. Ed.*, 2024, **63**, e202409200.

14. C. Cai, G. Yao, Y. Zhang, S. Zhang, F. Li, Z. Tan, and S. Dong, *Mater. Horiz.*, 2024, **11**, 5732-5739.